

Sensitivity of Nocturnal Boundary Layer to Tropospheric Aerosol Radiative Forcing Under Clear Sky Conditions

Udaysankar S. Nair¹, Richard McNider², Falguni Patadia¹, Sundar A. Christopher^{1,2} and
Kirk Fuller¹

¹Earth System Science Center, University of Alabama in Huntsville, 320 Sparkman Drive
Huntsville, Alabama 35805

²Department of Atmospheric Science, University of Alabama in Huntsville
320 Sparkman Drive
Huntsville, Alabama 35805

Journal of Geophysical Research

December 17, 2009

Revised, February 17, 2010

¹ Corresponding Author: U.S. Nair, Earth System Science Center, University of Alabama in Huntsville, Huntsville, AL 35805 E-mail: nair@nsstc.uah.edu Phone: 256-961-7841

ABSTRACT

1
2
3 Since the middle of the last century, global surface air temperature exhibits an increasing trend,
4 with nocturnal temperatures increasing at a much higher rate. Proposed causative mechanisms
5 include the radiative impact of atmospheric aerosols on the nocturnal boundary layer (NBL)
6 where the temperature response is amplified due to shallow depth and its sensitivity to potential
7 destabilization. A one-dimensional version of the Regional Atmospheric Modeling System
8 (RAMS) is used to examine the sensitivity of the nocturnal boundary layer temperature to
9 surface longwave radiative forcing (SLWRF) from urban aerosol loading and doubled
10 atmospheric carbon dioxide concentrations, for typical mid-latitude nocturnal boundary layer
11 case days from the CASES-99 field experiment. The analysis is further extended to urban sites
12 in Pune and New Delhi, India. For the cases studies, locally the nocturnal SLWRF from urban
13 atmospheric aerosols ($2.7 - 30 \text{ W m}^{-2}$) is comparable or exceeds that caused by doubled
14 atmospheric carbon dioxide (3 W m^{-2}), with the surface temperature response ranging from a
15 compensation for daytime cooling to an increase in the nocturnal minimum temperature. The
16 sensitivity of the NBL to radiative forcing is approximately four times higher compared to the
17 daytime boundary layer. Nighttime warming or cooling may occur depending on the nature of
18 diurnal variations in aerosol optical depth (AOD). Soil moisture also modulates the magnitude
19 of SLWRF, decreasing from 3 W m^{-2} to 1 W m^{-2} when soil saturation increases from 37% to
20 70%. These results show the importance of aerosols on the radiative balance of the climate
21 system.

22 **1 Introduction**

23 Surface air temperature observations in the last century show a clear trend of
24 nighttime minimum temperatures increasing at a rate twice that of the daytime maximum
25 temperature except during the 1979-2004 time period when the rate of increase of both
26 maximum and minimum temperatures are approximately the same [*Dai et al.* 1999; *Karl*
27 *et al.* 1984, 1993]. This asymmetry in the trends of maximum and minimum temperatures
28 have decreased the diurnal temperature range (DTR) over the land surface throughout the
29 globe with the exception of weak increases in central Canada and southeastern Australia
30 [*Karl et al.* 1993]. While the DTR decrease is present in every season, in most areas the
31 largest decreases occur during the Northern Hemisphere Summer and Fall seasons. There
32 is considerable debate regarding the mechanisms responsible for the DTR decrease
33 [IPCC 2007; *Dai et al.* 1999]. Some suggested factors responsible for this increase
34 include urban heat islands, greenhouse gases, clouds, land use changes, and tropospheric
35 aerosols [*Balling et al.*, 2003, *Braganza et al.*, 2004a; *Kalnay and Cai*, 2003; *Pielke et*
36 *al.*, 2007; *Zhou et al.*, 2007]. Heat island effects would initially appear to be a viable
37 mechanism because minimum temperatures are more susceptible to urban thermal inertia.
38 However, DTR climate trend analyses often attempt to remove these urban effects [*Karl*
39 *et al.*, 1984].

40 Global Circulation Model (GCM) sensitivity studies show that increased
41 concentration of greenhouse gases such as CO₂ and CH₄ also cause changes in DTR.
42 However, comparative studies with state-of-the-art GCMs reveal differences in the
43 magnitude and even the sign of DTR trends among the models. These studies also reveal
44 large discrepancies between modeled and observed DTR trends [*Karl et al.*, 1993]. Based

45 on these results, *Karl et al.* [1993] and *Stone and Weaver* [2003] concluded that the land
46 surface parameterizations or physics in existing GCMs may not be robust enough to
47 correctly capture the observed DTR signal. *Walters et al.* [2007] also proposed that the
48 coarse resolution in GCMs may not correctly capture the sensitivity of the nocturnal
49 boundary layer to either external forcing or parameters describing the land surface
50 characteristics.

51 Cloudiness trend is another factor that needs to be considered in interpreting
52 observed DTR trends. *Dai et al.* [1999] examined the physical and statistical relationships
53 of clouds, precipitation, and soil moisture in the First International Satellite Land Surface
54 Climatology Project (ISLCP) Field Experiment (FIFE) data. They showed that clouds
55 could change the DTR, and that soil moisture was less important than clouds. Using this
56 evidence, and some historical measures of cloudiness trends, they concluded that
57 cloudiness was the most likely cause of the DTR change. *Hansen et al.* [1995] showed
58 that clouds were apparently the only adjustable GCM parameter that could damp the
59 DTR to its observed magnitude. However, the GCMs often lack adequate vertical
60 resolution in the nocturnal boundary layer (NBL) and do not include explicit treatment of
61 aerosol microphysics. As will be shown in this paper, aerosols would provide a similar
62 response signal to that of a change in cloudiness. Further, while cloudiness trends are
63 uncertain, anthropogenic aerosol loading in the atmosphere has definitively increased in
64 the last century [*Ramanathan et al.*, 2001a]. Recently, [*Kalnay and Cai*, 2003] conducted
65 a long-term reanalysis of modeled and observed data. This study showed that changes in
66 land surface usage, including irrigation, contribute significantly to the observed DTR
67 trends. Irrigation would have the expected effect of lowering daytime temperatures due to

68 evaporation, and raising nighttime temperatures due to the higher heat capacity of wet
69 soils and well-hydrated vegetation. However, rigorous statistical verification of this
70 mechanism would be difficult because surface moisture availability is not routinely
71 measured. Moreover, the DTR has decreased in some areas where irrigation effects
72 would be minimal, such as the eastern United States. All in all, with the uncertainties in
73 long-term cloudiness trends and the persistent deficiencies in GCM surface land
74 processes, there is still considerable uncertainty in explaining the DTR trends.

75 Increases in tropospheric aerosol concentrations have also been suggested as a
76 significant factor in the DTR trends [*Stone and Weaver, 2003; Braganza et al., 2004a,*
77 *2004b; Makowski et al., 2008*]. *Makowski et al.* [2008] attributes long-term trends in
78 DTR mostly to modulation of incoming solar radiation through the direct and indirect
79 aerosol effect. Most aerosol studies [*IPCC, 2007*] have concentrated on the direct
80 radiative effect of aerosol scattering and the indirect effects of aerosols in clouds [see *Yu*
81 *et al., 2002* for a comprehensive review]. Both effects tend to increase the planetary
82 albedo and reduce daytime temperatures. Recent global-scale aerosol studies [*Koch et al.,*
83 *2007*] have begun to demonstrate the importance of carbonaceous aerosols, especially
84 elemental carbon (EC), to the atmospheric aerosol budget. EC aerosols serve as net
85 warmers of the planetary boundary layer (PBL) and the free troposphere. This effect
86 would counter aerosol cooling in the daytime and reduce surface cooling at night.
87 Detailed reviews of aerosol measurement and modeling studies [*IPCC, 2007*] have
88 concluded that the foregoing aerosol effects are potentially significant (with magnitudes
89 comparable to the predicted warming from greenhouse gases), but also very poorly

90 understood (the magnitude of the net uncertainty is comparable to the aerosol effects; the
91 sign is unknown).

92 The majority of research studies on aerosol radiative interactions focus on the
93 daytime interaction of aerosols with solar radiation through both direct and indirect
94 pathways. However, there are relatively few studies that address the radiative impact of
95 aerosols on the nocturnal boundary layer [*Estournel et al.*, 1983; *Garratt et al.*, 1990;
96 *Jacobson*, 1997; *Venkatram and Viskanta*, 1977; *Yu et al.*, 2002; *Zdunkowski et al.*,
97 1976]. Even though these studies address various aspects of aerosol radiative interaction
98 with NBL, a systematic analysis that includes spatio-temporal variations of the NBL and
99 aerosols is lacking. *Zdunkowski et al.* [1976] conducted a detailed analysis of the impact
100 of air pollution on PBL including the hygroscopic growth of aerosols. While the
101 numerical modeling experiments of *Zdunkowski et al.* [1976] did not explicitly consider
102 effects of diurnal asymmetries in atmospheric aerosol loading [diurnal variations in
103 aerosol optical depth (AOD) resulting from changes in aerosol mass concentration,
104 chemical composition, particle size, etc.], they noted that dense haze cover at nighttime
105 following a clear day will lead to warming at the surface. *Jacobson* [1997] used a detailed
106 air pollution modeling system to examine the impact of aerosols on the PBL, including
107 the nocturnal effects. Even though the modeling system captured the diurnal variability of
108 aerosol loading, the study did not focus on the role of nocturnal heating and DTR trends.

109 It is the purpose of this study to investigate the response of the nocturnal boundary
110 layer to longwave aerosol radiative forcing. Simple models [*Pielke and Matsui*, 2005]
111 have indicated that due to the shallow nature of the nocturnal boundary layer under light
112 winds, the temperature response to longwave forcing may be large. Additionally,

113 *Walters et al.* [2007] showed that the forcing itself may change the boundary layer height
114 causing a mixing of heat down from aloft. This mixing of heat from aloft acts as a
115 multiplier effect to the direct warming due to the added radiation. While both of these
116 studies dealt with increases in downward longwave radiation into the surface from
117 greenhouse gases, similar responses might be expected from downward longwave
118 radiation to the surface from aerosols. Also, both of these studies employed simple
119 models. *Pielke and Matsui* [2005] employed a semi-empirical analytical formulation that
120 did not incorporate full nonlinear dynamics between the surface and the atmosphere.
121 *Walters et al.* [2007], while including full nonlinear interaction with the surface, only
122 employed a two-layer atmosphere. The present study will examine the response of a full
123 nonlinear multi-level atmospheric model (a one-dimensional version of the Regional
124 Atmospheric Modeling System - RAMS) to aerosol radiative forcing. The experimental
125 design and description of the numerical modeling system used are described in section 2,
126 while results, discussion of the analysis and conclusions are presented in sections 3, 4 and
127 5 respectively.

128 **2 Methodology**

129 **2.1 Experimental Design**

130 The primary goal of this study is to assess the immediate direct effect of surface
131 longwave radiative forcing (SLWRF) from urban aerosols on nighttime surface air
132 temperatures and gain an understanding of conditions and processes through which
133 surface air temperature is impacted. Also of interest is to compare the impact of SLWRF
134 from atmospheric aerosols to doubled atmospheric carbon-dioxide. This is achieved by
135 conducting sensitivity analysis on typical cases of observed, stable nocturnal boundary

136 layer (SNBL) development using a one-dimensional version of RAMS. While this study
137 is a sensitivity analysis, it is important to note that the experiments are based on a
138 nocturnal boundary layer that has the physical attributes of observations. As noted by
139 *Steenefeld et al.* [2006] and *Walters et al.* [2007], models often have difficulties
140 capturing the dynamic range of boundary layer cooling at night due to anomalous
141 numerical diffusion or profile formulations that preclude strong stability. Such models
142 will not be sensitive in resolving the effects of relatively small perturbations in longwave
143 radiation at the surface. Thus, this study adopts an experimental design where RAMS is
144 used to simulate typical SNBL case study days of 21-22 October 1999 from the
145 Cooperative Atmosphere-Surface Exchange Study [*Poulos et al.*, 2002] held in 1999
146 (CASES-99) near Leon, Kansas (37.65°N, 96.73°W) with the objective of improving the
147 understanding of processes relevant to the SNBL. The days used in this study are typical
148 SNBL case days that are the focus of other modeling studies [*Steenefeld et al.*, 2006].
149 The experimental design utilized in this study establishes the capability of the model to
150 faithfully simulate these typical SNBL case days by comparing model simulations against
151 detailed field observations of surface meteorology and energy fluxes collected during
152 CASES-99.

153 Sensitivity experiments are then conducted for these case days by modifying the
154 validated control experiment (C1), by including radiative forcing from typical urban
155 aerosols (U1) and doubled atmospheric carbon dioxide (X2, see Table 1 for description of
156 all the experiments). Additional sensitivity experiments, U2 and U3 are conducted to
157 examine the impact of diurnal variation in atmospheric aerosol loading, D1 to address the
158 impact of other aerosol types on SNBL development, while C2 and U4 are used to

159 examine how soil moisture modulates the impact of aerosol surface radiative forcing on
160 surface air temperature.

161 The analysis is then extended to urban locations where detailed observations are
162 not available for initialization and validation, but for which aerosol characterization is
163 available. The experiments U5 and U6, utilize urban aerosol composition characteristic
164 of two urban sites in India, namely Pune [*Panicker et al.*, 2008] and New Delhi [*Singh et*
165 *al.*, 2005] respectively, valid for the time period December 2004-January 2005 and April-
166 June, 2003 respectively. The U5 and U6 experiments are compared against C3 and C4
167 which are experiments that are identical to U5 and U6, except for the assumption of clear
168 air conditions in order to examine whether the results obtained for CASES-99 site is also
169 applicable to other areas.

170 Note that the experiments used in this study are not climate experiments since
171 they do not look at the cumulative impact of either aerosols or greenhouse gases. Rather,
172 they provide an examination of the direct sensitivity of NBL to these forcings.

173 **2.2 Description of RAMS**

174 This study utilizes RAMS, Version 4.4, modified to include radiative interactions
175 of aerosols, to study the impact of aerosols on nocturnal boundary layer development.
176 RAMS is a nonhydrostatic atmospheric model used to simulate a wide range of
177 atmospheric phenomenon [*Cotton et al.*, 2003] and utilizes finite difference
178 approximations to solve conservation equations of mass, momentum, heat, and different
179 water phases. Cloud and precipitation processes are represented in the model through
180 either convective parameterization or explicit parameterization of cloud microphysics.
181 RAMS provides a variety of options with varying sophistication for representing subgrid-

182 scale turbulence. Land surface processes are simulated using a multi-layer soil model
183 and the Land Ecosystem Atmosphere Feedback (LEAF-2) model [*Walko et al.*, 2000].
184 While radiative transfer schemes of varying complexity [*Mahrer and Pielke*, 1977; *Chen*
185 *and Cotton*, 1983; *Harrington et al.*, 1999] are available in RAMS, none account for
186 radiative interactions with aerosols. RAMS was modified to include a Delta four-stream
187 radiative transfer scheme of *Fu and Liou* [1993], referred from hereon as FL-RTS [*Wang*
188 *and Christopher*, 2006; *Wang et al.*, 2006]. Aerosol characterization within FL-RTS is
189 based on the Optical Properties of Aerosols and Clouds (OPAC) based on *Hess et al.*
190 [1998].

191 **2.2.1 The FL-RTS**

192 The FL-RTS is a plane-parallel radiative transfer model [*Fu and Liou*, 1993] that
193 computes upwelling and downwelling radiative fluxes at specified, discrete locations
194 within an atmospheric column. The FL-RTS divides the radiation spectrum into six
195 broadbands in the shortwave (SW) part (0.2-4 μm), with the first bands (0.2-0.7 μm)
196 being subdivided into ten subbands. The longwave (LW) part of the spectrum (4-37.5
197 μm) is subdivided into twelve broadbands. Gaseous absorption characteristics within
198 these bands are computed using the correlated k-distribution method [*Fu and Liou*, 1992].
199 A delta function is used to model the forward scattering by clouds and aerosols. The FL-
200 RTS provides the option to be configured either in the two or four stream mode for
201 radiative flux computations. *Fu and Liou* [1993] show that the FL-RTS irradiance
202 estimates are within 0.05% of line-by-line calculations.

203 2.2.2 The OPAC Aerosol Types

204 The OPAC is a software package for specifying optical properties of clouds and
205 aerosols as a function of wavelength. Single scattering albedo (ω_o), asymmetry parameter
206 (g) and extinction coefficient (β_{ext}), for individual aerosol components and aerosol types
207 (mixture of components), are available at 61 wavelengths between 0.25 and 40 μm and at
208 eight relative humidity values between 0–99%. These optical properties along with
209 vertical distribution information are needed to specify aerosol radiative interactions in the
210 model. The OPAC assumes a lognormal size distribution for aerosols and optical
211 properties of individual components are computed assuming number concentrations of 1
212 cm^{-3} and therefore require appropriate scaling for differing situations. Aerosol types in
213 OPAC range from clean and polluted continental conditions to Arctic and Antarctic types
214 which are composed of specific mixes of individual components. The OPAC aerosol
215 types utilized in this study, namely Urban and Desert types differ both in composition
216 and microphysics (Table 2). Urban aerosol types have relatively high number
217 concentrations of water soluble and soot components, but smaller particle sizes in
218 comparison to desert aerosol types dominated by accumulation and coarse mode mineral
219 components (see Table 2). This study specifically focuses on Urban and Dust aerosol
220 types since prior studies report substantial SLWRF associated with these aerosol types
221 and thus the potential to impact SNBL evolution. The other two aerosol types considered
222 in study are essentially OPAC aerosol types modified to conform to characteristics of
223 urban aerosols observed over Pune and New Delhi, India, as reported in *Panicker et al.*
224 [2008] and *Singh et al.* [2005]. The aerosol type for Pune, India, valid for the time period
225 December 2003 through January 2004, is the OPAC Urban type with the number density

226 of the components modified (Table 2) to match the observed AOD, Single Scattering
 227 Albedo (SSA) and Asymmetry Parameter (ASP). Using a similar approach, *Singh et al.*
 228 [2005] found the pre-monsoon aerosol characteristics to be a mixture of the OPAC Urban
 229 and Desert aerosol types (Table 2).

230 2.2.3 Calculation of Aerosol Optical Thickness

231 Aerosol Optical Depth (AOD) is computed following *Hess et al.* [1998] by
 232 assuming exponentially decreasing number concentrations with height as given by
 233 equation 1:

$$234 \quad N(z) = N(0)e^{-\frac{z}{H}} \quad (1)$$

235 where z is the altitude above ground in kilometers and H is the scale height in kilometers.
 236 The scale height specifies the nature of decrease of number concentration with height,
 237 with increasing values describing smaller variation with height. Based on aerosol vertical
 238 distribution described by (1), AOD of an atmospheric layer contained between height
 239 levels z_1 and z_2 ($z_1 < z_2$) is given by:

$$240 \quad \tau_\lambda(z_1, z_2) = \int_{z_1}^{z_2} \beta_{ext}(z=0, \lambda, RH) e^{-\frac{z}{H}} dz = \beta_{ext}(z=0, \lambda, RH) H \left(e^{-\frac{z_1}{H}} - e^{-\frac{z_2}{H}} \right) \quad (2)$$

241 where λ is the wavelength, RH is relative humidity. For each aerosol type, OPAC outputs
 242 β_{ext} at $z = 0$, computed using specified number concentrations of individual components.
 243 OPAC specifies the total physical thickness of Urban and Desert aerosol layers as 2 and 6
 244 km and the scale heights to be 8 and 2 km respectively. Based on these parameters, the
 245 computed values of AOD at 0.55 μm and 80% RH for Urban and Desert aerosol types are
 246 0.643 and 0.286, respectively. The OPAC Urban AOD is consistent with values over

247 polluted regions in Africa, India, and China [*Ramanathan et al.*, 2001b; *Smirnov et al.*,
248 2002; *Pandithurai et al.*, 2007]. Since OPAC provides the optical properties only at eight
249 discrete RH values, linear interpolation is used to determine aerosol optical properties at
250 other RH values. Note, in addition to the mixed layer aerosol types, OPAC also suggests
251 the use of a background aerosol type for the free troposphere ($\tau \sim 0.013$), stratospheric
252 aerosol layer ($\tau \sim 0.005$), and if applicable, a transported mineral aerosol layer ($\tau \sim$
253 0.097). In this study, only the impact of the boundary layer aerosols is considered and the
254 effect of other categories is ignored.

255 **2.3 Numerical Model Configuration**

256 Numerical experiments consist of 1D simulations of atmospheric boundary layer
257 development over a 48-hour period starting from initial conditions characterized by
258 evening radiosonde observations. A pseudo one-dimensional configuration of RAMS to
259 simulate atmospheric boundary layer development using a domain of 5×5 grid points is
260 used with cyclic boundary conditions along the lateral boundaries. A sufficiently large
261 grid spacing of 10 km in the x and y directions is utilized so that the model is incapable
262 of resolving large eddies. Vertical grid structure, surface characteristics, and other
263 relevant information are provided in Table 3.

264 For the CASES-99 case days, when the soil model is directly initialized using soil
265 moisture observations, model-simulated latent heat fluxes are negligible compared to
266 observations. Latent heat flux observations are not negligible however, and thus suggest
267 that while the local soil moisture observations in the 0–25 cm layer are dry, it may not be
268 reflective of large-scale conditions. Therefore the soil moisture content in this layer was
269 systematically altered until close agreement was obtained between observations and

270 model-simulated sensible and latent heat fluxes, 2 m temperature, and relative humidity.
271 The altered soil moisture profile was utilized in all the other experiments.

272 In the urban site experiments (U5-U6), soil moisture and temperature
273 observations are not available and therefore information from the National Center for
274 Environmental Prediction (NCEP) Reanalysis dataset was utilized to initialize the soil
275 model. Note that the soil moisture values from the NCEP Reanalysis are average
276 conditions for 2.5×2.5 degree grid cell. Similar to C1 experiment, the soil moisture was
277 adjusted until there was relatively good agreement between the observed 2 m temperature
278 and relative humidity is obtained for U5 and U6 experiments.

279 **3 Results**

280 The sensitivity analyses discussed in the following sections utilize specific days
281 from CASES-99 (21-22 October 1999). Additional experiments conducted for the time
282 period 23-25 October 1999 CASES-99 days yielded similar results and thus are excluded
283 for brevity.

284 **3.1 Comparison of the CASES-99 Control Simulation to Observations**

285 Observations of downwelling solar radiation (Figure 1a) show the presence of
286 clouds in the time period centered around local solar noon on both 21 and 22 October
287 1999 making comparisons to model simulations complicated. Cloud cover appears to be
288 more optically thick and persistent on 21 October when compared to 22 October.
289 Comparison to observations on the 22 October shows the FL-RTS generally
290 overestimating the downwelling shortwave with a maximum difference of 61 W m^{-2} .
291 During the late afternoon hours for both days, when clouds are not present, mean error

292 between model simulation and observations is approximately 5%, slightly higher than the
293 than the 3% error estimated by *Christopher et al.* [2003].

294 Downwelling longwave radiation at the surface (Figure 1b) from FL-RTS
295 compare well with observations during both nights (differences of less than 2%), while
296 there are considerable differences during the first day (maximum of 18%). Significant
297 daytime differences during the first day may be related to the presence of clouds. During
298 the second night, there is again close agreement between model and observations with
299 differences averaging less than 2%. During the second day, there is better agreement
300 between the simulation and observations during the morning hours, but larger deviations
301 in the afternoon. However, note that there was a frontal passage through the area at this
302 time which the model does not capture.

303 There is good agreement between the observed and model-simulated upwelling
304 longwave radiation from the surface (Figure 1c), except during the afternoon hours of the
305 second day when the frontal passage occurred. Simulated patterns of surface sensible and
306 latent heat fluxes (Figure 1d,1e), though very similar to observations, lag the observations
307 by approximately half an hour. The heat and moisture fluxes show significant variability
308 during the first day due to cloudiness. During the second day, the variability is much less
309 and the maximum amplitudes of observed and simulated patterns of sensible and latent
310 heat fluxes differ by $\sim 40 \text{ W m}^{-2}$ and 15 W m^{-2} respectively. The RAMS simulations of
311 temperature and humidity patterns are also consistent with observations during the first
312 day, but differ during the second day due to frontal passage.

313 3.2 Radiative Impact of Urban Aerosols and Doubled Carbon Dioxide

314 While top-of-atmosphere shortwave and longwave radiative forcing metrics are
315 utilized in Earth radiation budget studies, radiative forcing at the surface is the metric that
316 is most relevant for this study. For given land surface conditions, the surface air
317 temperature, heat, and moisture fluxes to the atmosphere are most sensitive to net
318 radiative energy available at the surface. Thus surface shortwave and longwave radiative
319 forcing are the appropriate metrics for analyzing the impact of atmospheric aerosols on
320 boundary layer development and will be utilized in the analysis of the experiments
321 conducted in this study.

322 In the shortwave part of the spectrum, when comparing the control (C1), urban
323 aerosol (U1) and doubled CO₂ experiments (X2), significant differences are observed
324 only between the C1 and U1 experiments (Figure 2a). The downwelling shortwave
325 radiation at the surface is significantly reduced in the U1 experiment, with differences of
326 up to 123 W m⁻² occurring at the local solar noon hour. Since carbon dioxide is not a
327 major absorber in the shortwave, there is very little difference in the downwelling
328 shortwave flux at the surface between the X2 and C1 experiment.

329 However in the longwave there are significant differences between the U1, X2,
330 and the C1 experiment (Figure 2b). During the first night, both U1 and X2 show
331 enhancement in downwelling longwave of approximately 3.0 W m⁻² compared to the C1
332 experiment. During the second night, the enhancement in downwelling longwave in the
333 U1 simulation reduces to ~2.2 W m⁻². This reduction during the second night is related to
334 reduced water vapor loading in the U1 simulation due to attenuation of downwelling
335 shortwave radiation leading to less evaporation and transpiration. The nocturnal
336 enhancement in downwelling longwave radiation is within the range (2.5 to 16 W m⁻²)

337 reported by prior studies [*Estournel et al.*, 1983; *Jacobson*, 1997; *Panicker et al.*, 2008;
338 *Zdunkowski et al.*, 1976], closer to lower limits. The nighttime differences in
339 downwelling longwave between U1 and X2 are minimal during the first night ($\sim 0.1\text{--}0.2$
340 W m^{-2}) and are more significant during the second night ($\sim 1 \text{ W m}^{-2}$). During the daytime,
341 the differences in downwelling longwave between the C1 and U1 simulations are
342 significantly greater with a maximum value of approximately 4.5 W m^{-2} reflecting
343 differing vertical distributions of aerosols and carbon dioxide. Note that the urban
344 aerosols are confined to the lowest 2 km while carbon dioxide is assumed to be well
345 mixed through the depth of the model atmosphere. Thus, under clear-sky conditions,
346 carbon dioxide is able to better absorb and reradiate enhanced longwave emissions from
347 the surface and the PBL during the daytime.

348 **3.3 Impact of Urban Aerosols and Doubled Carbon Dioxide on Surface Air** 349 **Temperature**

350 In the CASES experiments, enhancement in nocturnal downwelling longwave
351 radiation due to urban aerosol loading and doubling of carbon dioxide leads to an
352 increase in surface air temperature during the first night (Figure 2c). The nocturnal
353 minimum is increased by $\sim 0.38^\circ\text{C}$ and 0.3°C during the first night in U1 and X2
354 experiments, respectively. During the first day of the simulation, significant reduction of
355 downwelling shortwave radiation at the surface is accompanied by reduction in daytime
356 surface air temperature in the U1 experiment with a maximum difference of $\sim 2^\circ\text{C}$
357 occurring in the afternoon (Figure 3). The surface air temperature in the X2 simulation
358 shows a very small increase when compared to the C1 simulation, with a maximum
359 difference of less than 0.16°C (Figure 3) occurring in the afternoon. Note that the small

360 increase in daytime surface air temperature in the X2 experiment is primarily due to
361 enhancement in downwelling longwave radiation at the surface.

362 The impact of doubled carbon dioxide on surface air temperature during the
363 second night is very similar to that found during the first night. The solutions of surface
364 air temperature are similar in both the C1 and X2 simulations, but start diverging later in
365 the night with the surface air cooling at a faster rate in the C1 simulation. Nocturnal
366 minimum temperature in the C1 simulation is smaller than that found in the X2 simulation
367 by $\sim 0.35^{\circ}\text{C}$. The net effect of doubled carbon dioxide on the surface air temperature cycle
368 is reduction of DTR (Figure 3), with the increase in the nocturnal minimum more than
369 compensating for the negligible increase in the daytime maximum temperature.

370 However, the behavior of the U1 simulation is considerably different on the
371 second night. The surface air temperature in the U1 simulation is initially cooler
372 compared to the C1 simulation, but the solutions converge to similar values at early
373 morning hours. Note that, unlike the first night, where the initial surface temperature was
374 the same for both the C1 and U1 simulations, the surface temperature is initially cooler in
375 the U1 simulation (Figure 2d). The surface temperatures in the U1 and C1 simulations
376 converge during the early morning hours. These patterns (Figure 2c, 2d) suggest that
377 daytime cooling of the surface during the first day leads to cooler surface air temperature
378 going into the second night and that the enhancement in downwelling longwave radiation
379 at the surface in the U1 simulation causes the nocturnal minimum temperature to be the
380 same as that in the C1 simulation. This is verified by the U2 simulation, where the
381 aerosol optical depth is set to zero at nighttime, which shows that without the longwave
382 enhancement (Figure 4a), surface air temperature remains cooler compared to the C1

383 simulation (Figure 4b), yielding lower nocturnal minimum temperatures (Figure 3) and
384 increase in DTR of $\sim 0.66^{\circ}\text{C}$ (Figure 3). RAMS simulation experiments show that the
385 impact of urban aerosols is to reduce the DTR by reducing the daytime maximum and by
386 increasing the nocturnal minimum temperature.

387 **4 Discussion**

388 RAMS simulations show that heavy aerosol loading and characteristics of
389 conditions in polluted regions around the globe such as India and China, have a
390 significant impact on surface air temperature and the radiation budget. Nocturnal SLWRF
391 due to heavy urban aerosol loading and direct radiative effects of doubled atmospheric
392 carbon dioxide at local scales are comparable for the cases considered in this study (see
393 section 3.2). Therefore, on a local scale, urban aerosols have the potential to impact
394 nocturnal boundary layer temperature. Since many of the temperature observations
395 around the globe used in the DTR trend analysis are made in urban settings, the local
396 effects may have a significant impact on such trends.

397 This study illustrates that the response of the SNBL surface air temperature to
398 perturbations in the surface radiation budget is disproportionate when compared to the
399 convective boundary layer (CBL). Nocturnal boundary layer processes and their
400 sensitivity to changes in both radiation input and surface properties are relevant to
401 interpreting trends in surface air temperature and DTR. Note that a nocturnally averaged
402 radiative forcing of 3.2 W m^{-2} resulted in an average surface air temperature increase of
403 0.22°C during the first night in the U1 experiment, while a daytime average radiative
404 forcing of -84 W m^{-2} leads to an average daytime surface air temperature cooling of

405 1.5°C. The sensitivity of surface air temperature to perturbations in downwelling
406 radiation (δ) due to urban aerosol loading may be quantified as:

$$407 \quad \delta = \frac{\Delta \bar{T}_a}{\Delta \bar{F}_\downarrow} \quad (3)$$

408 where $\Delta \bar{T}_a$ and $\Delta \bar{F}_\downarrow$ are average differences in surface air temperature and average
409 forcing of downwelling radiation at the surface due to urban aerosol loading. The δ
410 values computed separately for NBL (δ_{NBL}) and CBL (δ_{CBL}) occurring during the first 24
411 hours of the U1 simulation yields values of 0.068 and 0.018 K/W m⁻². Thus the sensitivity
412 of the SNBL surface air temperature to SLWRF radiative forcing from urban aerosol
413 loading is 3.7 times more than that of the CBL. This difference in sensitivity is largely
414 due to the differences in depth of the CBL and NBL. *Walters et al.* [2007] examined
415 temperature sensitivity of NBL to arbitrarily prescribed SLWRF using a two- layer
416 atmosphere and found a sensitivity of about 0.12 K/W m⁻² in the light wind very stable
417 NBL and about 0.04 K/W m⁻² in the weakly stable NBL (see discussion and Figure 7
418 below). Thus, the results of this more complete boundary layer model are in keeping with
419 the simple model employed by *Walters et al.* [2007]. The additional downward radiation
420 at the surface at night is smaller due to the radiating temperature of the lower part of the
421 atmosphere thus the actual increase downward radiation due to aerosols is larger than this
422 net change. However, the smaller depth of the NBL confines this heating to a smaller
423 depth [*Walters et al.*, 2007] leading to a larger temperature response and thus sensitivity.

424 In the specific cases considered in this study, the magnitude of daytime reduction
425 in surface air temperature dominates over the nocturnal warming leading to overall
426 cooling effect. However, the overall effect could be different depending on several

427 factors, including aerosol optical characteristics, diurnal variations in column loading and
428 vertical distribution, and nocturnal boundary layer dynamics. For example, in the model
429 simulations of *Jacobson* [1997] over the Los Angeles Basin, urban aerosols with
430 differing optical characteristics caused a daytime cooling of 0.08 K, a maximum
431 reduction in shortwave of 55 W m^{-2} (150 W m^{-2} in the present study), nocturnal warming
432 of 0.77 K and maximum nocturnal longwave enhancement of 13 W m^{-2} (4.0 W m^{-2} in the
433 present study). Other studies also report larger magnitudes for nocturnal enhancement of
434 longwave in the presence of urban aerosols [*Estournel et al.*, 1983; *Panicker et al.*, 2008;
435 *Welch and Zdunkowski*, 1976]. The study also examined the impact of other OPAC
436 aerosol models on boundary development and found desert aerosols to be the only type
437 capable of producing longwave forcing similar to *Jacobson* [1997]. The D1 simulation,
438 where the OPAC desert aerosol optical model is used, shows a nocturnal downwelling
439 longwave radiation increase of 9 W m^{-2} (Figure 2b) leading to nocturnal surface air
440 temperature increases of more than 1 K and a depression in DTR of $\sim 1.6^\circ\text{C}$ (Figure 4b).

441 Differences in nocturnal surface air temperature evolution between the first and
442 second nights in the U1 simulation (Figure 2c) resulting from differing amounts of
443 daytime surface heating, suggest that diurnal variations in aerosol column loading and
444 vertical distribution are important factors in determining the overall impact on DTR and
445 average surface air temperature. Constant aerosol composition and number
446 concentrations are assumed in the aerosol experiments used in this study and the temporal
447 variations in aerosol optical depth is solely due to the hygroscopic effect (Figure 6).
448 However, in reality, time-varying emissions and atmospheric circulation patterns lead to
449 diurnal asymmetries in aerosol composition, number concentrations and vertical

450 distribution [Allen et al., 1999; Dorsey et al., 2002; Guasta, 2002; Mårtensson et al.,
451 2006; Pandithurai et al., 2007; Smirnov et al., 2002]. Diurnal variation patterns of AOD,
452 where it is substantially higher during the early morning and late evening hours compared
453 to midday [Pandithurai et al., 2007], would lead to a reduction in cooling during daytime
454 and enhancement in nighttime warming. Enhancement in nighttime warming is also
455 expected for scenarios where there is an increase in black carbon concentrations during
456 the early morning hours [Allen et al., 1999] due to increased emissions from traffic and
457 trapping of aerosols. Other sites such as Mexico City [Smirnov et al., 2002] exhibit
458 patterns where the AOD increases during the afternoon hours thereby enhancing the
459 cooling effect of aerosols. The U3 simulation, in which the daytime AOD is reduced by a
460 factor of one-half, was used to examine the impact of the diurnal variation of AOD on
461 surface air temperature. Note that the U3 crudely mimics the AOD diurnal variation
462 reported by Pandithurai et al. [2007], where the AOD during the early morning or late
463 afternoon hours differs from midday values by a factor of two. Compared to the U1
464 simulation, the U3 simulation shows an increase in nocturnal surface air temperature
465 (Figure 5) with the nocturnal minimum temperature during the second night being higher
466 by $\sim 0.18^{\circ}\text{C}$ (Figure 3). However, the DTR in U3 simulation is higher by $\sim 0.79^{\circ}\text{C}$ due to
467 increase in incoming shortwave compared to the U1 simulation (Figure 3).

468 Relative humidity enhancement in NBL also creates diurnal asymmetries in AOD
469 as hygroscopic aerosols respond to a nighttime increase of RH and swell (Figure 6). The
470 impact of hygroscopic swelling in NBL is often insubstantial as the RH increase is
471 confined to a very shallow layer ($<100\text{ m}$), with the maximum swelling of the aerosols
472 occurring at the lowest model level (Figure 6). However, in situations where there are

473 substantial emissions of aerosols into the NBL, significant day-night differences in
474 vertical distribution of aerosols exist [Guasta, 2002] and the hygroscopic effect could be
475 important depending upon aerosol composition.

476 The magnitude of δ_{NBL} , and thus response of DTR and mean surface air
477 temperature to aerosol radiative forcing, is strongly dependent on NBL dynamics [Dai
478 and Trenberth, 2004; Pielke and Matsui, 2005; Walters *et al.*, 2007]. A recent study by
479 Walters *et al.* [2007] used nonlinear analysis techniques to examine the sensitivity of the
480 stable nocturnal boundary layer (SNBL) to perturbations in incoming longwave radiation
481 and surface characteristics. Walters *et al.* [2007] found perturbations that decrease NBL
482 stability lead to significant increases in surface temperature. Increase in turbulence that
483 accompany the decrease in NBL stability lead to mixing of warm air from aloft causing
484 rapid, significant changes in surface air temperature. Average longwave nocturnal
485 radiative forcing of 3.0 W m^{-2} found in U1 simulations is within the range of
486 perturbations found by Walters *et al.* [2007] to be capable of substantially altering the
487 surface air temperature in the NBL through destabilization. However, the present study
488 may not likely fully capture the destabilization of the NBL as reported by Walters *et al.*
489 [2007] since the destabilization only occurs when the NBL is near a threshold of
490 transitioning between a strongly stable NBL and weakly stable NBL. Figure 7, created
491 using the bifurcation diagram techniques reported in Walters *et al.* [2007] illustrates this
492 potential transition. Under light winds (Figure 7a) the additional downward radiation
493 produces an increasing temperature in the NBL with a slope (or sensitivity as discussed
494 above) of about 12 K/W m^{-2} . Under strong winds, when the NBL depth is greater, the
495 simple model indicates less sensitivity. However, at intermediate winds, the temperature

496 difference between the two states can be of order 7–9 K and a sensitivity of 0.28–0.36
497 K/W m⁻². Based on the shape of the temperature time series, the first CASES night is
498 probably within the strongly stable case and the second night not quite as stable.
499 However, it may be that the roughness and wind speed are not at the transition parameter
500 space discussed by *Walters et al.* [2007] which can lead to amplified sensitivity. Thus, it
501 may be that other nights may be at this transitional threshold. Only a few nights each year
502 when the aerosols cause the transition to a warmer boundary layer may produce a larger
503 climatological temperature difference than reported here.

504 Soil moisture impacts the partitioning of net radiation received at the surface and
505 thus plays an important role in the diurnal evolution of surface air temperature. Since the
506 soil moisture determines the amount of water vapor added to the boundary layer during
507 the day, it also modulates the aerosol radiative longwave radiative forcing. In order to
508 examine the impact of soil moisture on aerosol nocturnal longwave radiative forcing, the
509 C1 and U1 simulations were repeated with soil saturation increased uniformly throughout
510 the depth of the soil layer to 70%, referred hereon as C2 and U4 simulations. Differences
511 in downwelling longwave radiation between C2 and U4 (Figure 8a) during the second
512 night are significantly smaller compared to differences found in the C1 and U1
513 simulations (Figure 2b). The decrease in nocturnal radiative forcing occurs in the higher
514 soil moisture situation because the C2 simulation develops a substantially moister
515 boundary layer compared to the U3 simulation during the first day. Enhancement of
516 water vapor in the C2 simulation leads to an increase in downwelling longwave radiation
517 partially offsetting the increase in downwelling longwave radiation in U3 from aerosol
518 loading resulting in a smaller nocturnal SLWRF. Interestingly, comparison of surface air

519 temperature between the C2 and U4 simulations show slight nocturnal warming in the U4
520 simulation during parts of the second night (Figure 8b). The reason for this behavior is
521 not understood and illustrates the complex nonlinear interactions exhibited by the NBL
522 dynamics.

523 Of all the experiments considered, the C2 and U4 show the most dramatic change
524 in DTR when compared to C1 (Figure 3). The difference in DTR between C2, U4, and
525 C1 are -7.3 and -8.4 °C while the DTR differences between other experiments and C1 are
526 in the range -0.2 to -2 °C. When compared to C1, even though the daytime maximum
527 temperature in the C2 and U4 experiments are reduced by more than -5.9 °C, the
528 nocturnal minimum temperature is higher in C2 and U4 by more than 1.2 °C. The reason
529 for this strong nocturnal warming, despite strong surface air cooling during the daytime,
530 is due to a combination of factors including increased soil heat capacity and bare soil
531 emissivity and an increase in boundary layer moisture during the second day. The impact
532 of enhanced boundary layer moisture in the C2 and U4 experiments is obvious during the
533 second night when the maximum differences in downwelling longwave radiation between
534 both these experiments and C1 exceed 6 W m^{-2} . *Christy et al.* [2006] found an increasing
535 trend in the nocturnal minimum temperature in irrigated regions of central California and
536 suggested changes in soil heat capacity and enhanced water vapor concentration in the
537 boundary layer as possible reasons. The C2 and U4 experiments in this study do indeed
538 support this hypothesis.

539 The validity of results obtained from the sensitivity analysis for CASES-99 days
540 is further tested in numerical experiments U5 (Pune, 19-21 January 2005) and U6 (Delhi,
541 30 May 2003) where urban land surface characteristics and aerosol optical characteristics

542 deduced from observations are imposed. For the Pune site, the U5 and C3 experiments
543 show nocturnal SLWRF of $\sim 4.7 \text{ W m}^{-2}$ and 2.7 W m^{-2} during the first and second night
544 respectively (Figure 9a) which is not substantially different than that found for CASES-99
545 sensitivity analysis. Comparison of the U6 and C4 experiments for the Delhi site show
546 nocturnal SLWRF of 28.5 W m^{-2} and 29.7 W m^{-2} during the first and second night
547 respectively (Figure 9c), which is significantly higher than that found in all the other
548 experiments. Note that the higher values of nocturnal SLWRF for the Delhi site is partly
549 due to substantially higher surface temperatures compared to other experiments. The
550 response of 2 m temperature to urban aerosol SLWRF at the Pune site is an increase in
551 nocturnal minimum of 0.51°C and 0.12°C during the first and second nights respectively
552 and a decrease in DTR of 0.72°C (Figure 9b). At the Delhi site, the SLWRF leads to an
553 increase in nocturnal minimum of 1.14°C and 1.69°C during the first and second nights
554 respectively and a decrease in DTR of 3.07°C (Figure 9d). Note the experiments were
555 repeated for five other selected days selected for each of the urban sites with similar
556 results. These experiments show that there is considerable variability in the magnitude of
557 nocturnal SLWRF resulting from urban aerosols, compensating for the daytime cooling at
558 the minimum (Figure 9b, Figure 9d) or causing significant nighttime warming on the
559 extreme.

560 Note that the numerical modeling experiments exhibit differing responses of
561 SLWRF and nocturnal warming to variations in aerosol microphysics and composition.
562 The composition and microphysics of aerosols in the U1 experiment are such that it
563 substantially impacts both the downwelling shortwave and longwave radiation. Water
564 soluble aerosols components (nitrates and sulfates) in the U1 experiment, with smaller

565 particle size and large number concentrations, lead to significant reduction in daytime
566 downwelling shortwave due to scattering. The soot aerosol component (black carbon) in
567 U1 experiment contributes to absorption in both shortwave and longwave part of the
568 spectrum. In contrast, the coarse mode mineral component with larger particle sizes in
569 the D1 and U6 experiments are substantially more effective absorbers of longwave
570 radiation and leads to higher values of SLWRF that overwhelm the cooling caused the
571 daytime reduction in downwelling shortwave radiation.

572 The numerical experiments considered in this study show a complex response of
573 diurnal surface air temperature variation to urban atmospheric aerosol loading (Figure 3).
574 It is essential to consider aerosol impacts when interpreting surface temperature records
575 in areas such as China, India, and Africa. However, accounting for the aerosol
576 contribution is difficult since the surface air temperature response is dependent on spatial
577 and temporal variations in aerosol concentration, optical characteristics, and is also
578 modulated by other factors such as soil moisture, land surface characteristics, etc.

579 **5 Conclusions**

580 Aerosol radiative forcing plays an important role on the boundary layer
581 development and surface temperature evolution. In the context of global climate change,
582 there is considerable interest on the role of aerosols in the climate system especially
583 surface temperature. Previous focus of the research effort in this area has been on
584 shortwave radiative forcing with little attention paid to the impact of longwave radiative
585 forcing which may be amplified through nocturnal boundary layer dynamics. Since there
586 is a disproportionate nocturnal contribution to warming trends detected in surface
587 temperature records [Karl *et al.*, 1993], it is important to understand the impact of aerosol

588 radiative forcing on nocturnal boundary layer development. This study uses two typical
589 cases of SNBL from the CASES-99 field experiment to examine the impact of urban
590 aerosol radiative forcing on SNBL. For the case study days considered in this study, it is
591 found that:

- 592 1. Urban aerosols have a nocturnal downwelling longwave radiative forcing impact
593 at the surface similar to that from doubled atmospheric carbon dioxide at local
594 scales. Enhanced nocturnal downwelling longwave from urban aerosols
595 compensate for the daytime cooling due to a reduction in downwelling solar
596 radiation. When diurnal variations in AOD are minimal, urban aerosols maintain
597 the nocturnal minimum surface air temperature the same as that found for clear
598 atmosphere even though the daytime maximum is higher for clear sky conditions.
- 599 2. Sensitivity of surface air temperature to radiative forcing is higher by a factor of
600 more than three in the NBL compared to CBL since the energy changes impact a
601 shallower layer during the nighttime.
- 602 3. Aerosol radiative characteristics and diurnal asymmetries in AOD play an
603 important role in determining the overall impact of aerosols on surface air
604 temperature.
- 605 4. An increase in downwelling longwave radiation at the surface caused by urban
606 aerosols is of sufficient magnitude to cause destabilization of the marginally
607 stable NBL and significant surface air temperature fluctuations from enhanced
608 vertical mixing as suggested by *Walters et al.* [2007].
- 609 5. The impact of urban aerosol longwave radiative forcing is strongly modulated by
610 soil moisture. SLWRF due to urban aerosols decreases for conditions of higher

611 soil moisture. This is because with higher soil moisture conditions, the boundary
612 layer water vapor content is enhanced under clear sky conditions, leading to an
613 increase in downwelling longwave at the surface.

614 In order to understand the impact of urban aerosols on surface air temperature and
615 DTR, detailed knowledge regarding diurnal variation of aerosol characteristics including
616 vertical distribution, optical properties, and column loading are needed. Further modeling
617 studies are necessary to examine the impact of aerosol radiative forcing on the marginally
618 stable NBL. Once the NBL conditions most sensitive to urban aerosol radiative forcing
619 are identified, the frequency of occurrence of such conditions needs to be determined
620 from observations. Such analysis will allow quantification of the aerosol radiative forcing
621 contribution to observed nocturnal warming trends.

622

623 **Acknowledgements**

624 This research was supported by DOE grant DE-FG02-05ER45187 and NSF grant
625 ATM-0417774 Dr. Sundar Christopher was supported by NASA Radiation Sciences
626 Program.

627

References

- 628 Allen, G. A., J. Lawrence, and P. Koutrakis (1999), Field validation of a semi-continuous
629 method for aerosol black carbon (aethalometer) and temporal patterns of
630 summertime hourly black carbon measurements in southwestern PA, *Atmos.*
631 *Environ.*, *33*, 817-823, doi:10.1016/S1352-2310(98)00142-3.
- 632 Balling, R. C., Jr., and R. S. Cerveny (2003), Vertical dimensions of seasonal trends in
633 the diurnal temperature range across the central United States, *Geophys. Res.*
634 *Let.*, *30*(17), 1878, doi:10.1029/2003GL017776
- 635 Braganza, K., D.J. Karoly, and J.M. Arblaster (2004a), Diurnal temperature range as an
636 index of global climate change during the 20th century, *Geophys. Res. Let.*, *31*,
637 10.1029/2004GL019998.
- 638 Braganza, K., D.J. Karoly, A.C. Hirst, A.C. Hirst, P. Stott, R.J. Stouffer, and S.F.B. Tett
639 (2004b) Simple indices of global climate variability and change: Part II -
640 Attribution of climate change during the 20th century, *Climate Dyn.*, *22*, 823-838,
641 10.1007/s00382-004-0413-1.
- 642 Chen, C., and W. R. Cotton (1983), A one-dimensional simulation of the stratocumulus-
643 capped mixed layer, *Boundary-Layer Meteorol.*, *25*, 289-321, DOI:
644 10.1007/BF00119541.
- 645 Chen, F., K.W. Manning, S.B. LeMone, J.G. Alfieri, R. Roberts, M. Tewari, D. Niyogi,
646 T.W. Horst, S.P. Oncley, J. Basara, P.D. Blanken (2007), Description of
647 Evaluation of the Characteristics of the NCAR High-Resolution Land Data
648 Assimilation System During IHOP-02. *J. Appl. Meteorol.*, *46*, 694-713, DOI:
649 10.1175/JAM2463.1.

650 Christopher, S.A., J. Wang, Q. Ji, and S-C. Tsay (2003), Estimation of shortwave dust
651 aerosol radiative forcing during PRIDE, *J. Geophys. Res.*, *108(D19)*, 8956,
652 doi:10.1029/2002JD002787.

653 Christy, J. R., W. B. Norris, K. Redmond, and K. P. Gallo (2006), Methodology and
654 results of calculating central California surface temperature trends: Evidence of
655 human-induced climate change? *J. Climate*, *19*, 548-563, DOI:
656 10.1175/JCLI3627.1.

657 Cotton, W. R., R. A. Pielke, R. L. Walko, G. E. Liston, and C. J. Tremback (2003),
658 RAMS 2001: Current status and future directions, *Meteorol. Atmos. Phys.*, *82*, 5-
659 29, 10.1007/s00703-001-0584-9.

660 Dai, A., and K. E. Trenberth (2004), The diurnal cycle of its depiction in the Community
661 Climate System Model, *J. Climate*, *17*, 930-951.

662 Dai, A., Kevin E. Trenberth, and T. R. Karl (1999), Effects of clouds, soil moisture,
663 precipitation, and water vapor temperature range, *J. Climatol.*, *12*, 2451-2473,
664 DOI: 10.1175/1520-0442(2004)017<0930:TDCAID>2.0.CO;2.

665 Dorsey, J. R., E. Nemitz, M. W. Gallagher, D. Fowler, P. I. Williams, K. N. Bower, and
666 K. M. Beswick (2002), Direct measurements and parameterisation of aerosol flux,
667 concentration and emission velocity above a city, *Atmos. Environ.*, *36*, 791-800,
668 doi:10.1016/S1352-2310(01)00526-X.

669 Estournel, C., R. Vehil, D. Guedalia, J. Fontan, and A. Druilhet (1983), Observations and
670 modeling of downward radiative fluxes (solar and infrared) in urban/rural areas, *J.*
671 *Climate Appl. Meteorol.*, *22*, 134-142, DOI: 10.1175/1520-
672 0450(1983)022<0134:OAMODR>2.0.CO;2.

673 Fu, Q., and K. N. Liou (1992), On the correlated k-distribution method for radiative
674 transfer in nonhomogeneous atmospheres, *J. Atmos. Sci.*, *49*, 2139-2156, DOI:
675 10.1175/1520-0469(1992)049<2139:OTCDMF>2.0.CO;2.

676 — (1993) Parameterization of the radiative properties of cirrus clouds, *J. Atmos. Sci.*,
677 *50*, 2008-2025, DOI: 10.1175/1520-0469(1993)050<2008:POTRPO>2.0.CO;2.

678 Garratt, J. R., A. B. Pittcock, and K. Walsh (1990), Response of the atmospheric boundary
679 layer and soil layer to a high altitude, dense aerosol cover, *J. Appl. Meteorol.*, *29*,
680 35-52, DOI: 10.1175/1520-0450(1990)029<0035:ROTABL>2.0.CO;2.

681 Guasta, M. D. (2002), Daily cycles in urban aerosols observed in Florence (Italy) by
682 means of an automatic 532-1064nm LIDAR, *Atmos. Environ.*, *36*, 2853-2865,
683 10.1016/S1352-2310(02)00136-X.

684 Hansen, J., M. Sato, and R. Ruedy (1995), Long-term changes of the diurnal temperature
685 cycle: Implications about mechanisms of global climate change, *Atmos. Res.*, *37*,
686 175-210, doi:10.1016/0169-8095(94)00077-Q.

687 Harrington, J. Y., T. Reisin, W. R. Cotton, and S. M. Kreidenweis (1999), Cloud
688 resolving simulations of Arctic stratus: Part II: Transition-season clouds, *Atmos.*
689 *Res.*, *51*, 45-75, doi:10.1016/S0169-8095(98)00098-2.

690 Hess, M., P. Koepke, and I. Schult (1998), Optical properties of aerosols and clouds: The
691 software package OPAC, *Bull. Am. Meteorol. Soc.*, *79*, 831-844, DOI:
692 10.1175/1520-0477(1998)079<0831:OPOAAC>2.0.CO;2.

693 IPCC (2007), *Climate Change 2007 - The Physical Science Basis: Working Group I*
694 *Contribution to the Fourth Assessment Report of the IPCC (Climate Change*
695 *2007)*. Solomon, S., D. Qin, M. Manning, Z. Chen, M. Marquis, K.B. Averyt, M.

696 Tignor and H.L. Miller (eds.), Cambridge University Press, Cambridge, United
697 Kingdom and New York, NY, USA.

698 Jacobson, M. Z. (1997), Development and application of a new air pollution modeling
699 system -- Part III. Aerosol-phase simulations, *Atmos. Environ.*, **31**, 587-608,
700 doi:10.1016/S1352-2310(96)00201-4.

701 Kalnay, E., and M. Cai (2003), Impact of urbanization and land-use change on climate,
702 *Nature*, **423**, 528-531.

703 Karl, T. R., G. Kukla, and J. Gavin (1984), Decreasing diurnal temperature range in the
704 United States and Canada from 1941 through 1980, *J. Climatol.*, **23**, 1489-1503,
705 DOI: 10.1175/1520-0450(1984)023<1489:DDTRIT>2.0.CO;2.

706 Karl, T. R., P. D. Jones, R. W. Knight, G. Kukla, N. Plummer, V. Razuvayev, K. P.
707 Gallo, J. Lindsey, R. J. Charlson, and T. C. Peterson (1993), A new perspective
708 on recent global warming: asymmetric trends of daily maximum and minimum
709 temperature, *Bull. Am. Meteorol. Soc.*, **74**, 1007-1023, DOI: 10.1175/1520-
710 0477(1993)074<1007:ANPORG>2.0.CO;2.

711 Koch, D., T. C. Bond, D. Streets, N. Unger, and G. R. v. d. Werf (2007), Global impacts
712 of aerosols from particular source regions and sectors, *J. Geophys. Res.*, **112**,
713 D02205, doi:10.1029/2005JD007024.

714 Mahrer, Y., and R. A. Pielke (1977), The effects of topography on sea and land breezes in
715 a two-dimensional numerical model, *Mon. Weather Rev.*, **105**, 1151-1162, DOI:
716 10.1175/1520-0493(1977)105<1151:TEOTOS>2.0.CO;2.

717 Makowski, K., M. Wild, and A. Ohmura (2008), Diurnal temperature range over Europe
718 between 1950 and 2005, *Atmos. Chem. Phys. Discuss.*, *8*, 7051-7084,
719 www.atmos-chem-phys.net/8/6483/2008/.

720 Mårtensson, E. M., E. D. Nilsson, G. Buzorius, and C. Johansson (2006), Eddy
721 covariance measurements and parameterisation of traffic related particle
722 emissions in an urban environment, *Atmos. Chem. Phys.*, *6*, 769-785, www.atmos-chem-phys.net/6/769/2006/.

724 Pandithurai, G., R. T. Pinker, P. C. S. Devara, T. Takamura, and K. K. Dani (2007),
725 Seasonal asymmetry in diurnal variation of aerosol optical characteristics over
726 Pune, western India, *J. Geophys. Res.*, *112*, D08208, doi:10.1029/2006JD007803.

727 Panicker, A. S., G. Pandithurai, P. D. Safai, and S. Kewat (2008), Observations of
728 enhanced aerosol longwave radiative forcing over an urban environment,
729 *Geophys. Res. Lett.*, *35*, L04817, doi:10.1029/2007GL032879

730 Pielke, R. A., and T. Matsui (2005), Should light wind and windy nights have the same
731 temperature trends at individual levels even if the boundary layer averaged heat
732 content change is the same? *Geophys. Res. Lett.*, *32*, L21813,
733 10.1029/2005GL024407.

734 Pielke Sr., R.A., C. Davey, D. Niyogi, S. Fall, J. Steinweg-Woods, K. Hubbard, Lin, M.
735 Cai, Y.-K. Lim, H. Li, J. Nielsen-Gammon, K. Gallo, R. Hale, R. Mahmood, S.
736 Foster, R. T. McNider, and P. Blanken (2007), Unresolved issues with the
737 assessment of multi-decadal global land temperature trends, *J. Geophys. Res.* *112*,
738 *D24S08*, doi:10.1029/2008JD008229.

739 Poulos, G. S., W. Blumen, D. C. Fritts, J. K. Lundquist, J. Sun, S. P. Burns, C. Nappo, R.
740 Banta, R. Newsom, J. Cuxart, E. Terradellas, B. Balsley, and M. Jensen (2002),
741 CASES-99: A comprehensive investigation of the stable nocturnal boundary
742 layer, *Bull. Am. Meteorol. Soc.*, 83, 555-581, DOI: 10.1175/1520-
743 0477(2002)083<0555:CACIOT>2.3.CO;2.

744 Ramanathan, V., P. J. Crutzen, J. T. Kiehl and D. Rosenfeld, (2001a), Aerosols, climate,
745 and the hydrological cycle, *Science*, 294, 2119-2124.

746 Ramanathan, V., P. J. Crutzen, J. Lelieveld, A. P. Mitra, D. Althause, J. Anderson, M. P.
747 O. Andreae, W. Cantrell, C.R. Cass, C.E. Chung, A.D. Clarke, J.A. Coakley,
748 W.D. Collins, W.C. Conant, F. Dulac, J. Heintzenberg, B. Holben, S. Howell, J.
749 Hudson, A. Jayaraman, J.T. Kiehl, T.N. Krishnamurti, D. Lubin, G. McFarquhar,
750 T. Novakov, J.A. Ogren, I.A. Podgorny, K. Prather, K. Priestley, J.M. Prospero,
751 P.K. Quinn, K. Rajeev, P. Rasch, S. Rupert, R. Sadourny, S.K. Satheesh, G.E.
752 Shaw, P. Sheridan, and F.P.J. Valero (2001b), Indian Ocean Experiment: An
753 integrated analysis of the climate forcing and effects of the great Indo-Asian haze,
754 *J. Geophys. Res.*, 106(D22), 28,371–28,398.

755 Singh, S., S. Nath, R. Kohli, and R. Singh, (2005), Aerosols over Delhi during pre-
756 monsoon months: Characteristics and effects on surface radiation forcing,
757 *Geophys. Res. Lett.*, 32, L13808, doi:10.1029/2005GL023062.

758 Smirnov, A., B. N. Holben, T. F. Eck, I. Slutsker, B. Chatenet, and R. T. Pinker (2002),
759 Diurnal variability of aerosol optical depth observed at AERONET (Aerosol
760 Robotic Network) sites, *Geophys. Res. Lett.*, 29(23), 2115,
761 doi:10.1029/2002GL016305.

762 Steeneveld, G. J., B. Wiel, and A. A. M. Holstag (2006), Modeling the evolution of the
763 atmospheric boundary layer coupled to the land surface for three contrasting
764 nights in CASES-99, *J. Atmos. Sci.*, *63*, 920-935, DOI: 10.1175/JAS3654.1.

765 Stone, D. A., and A. J. Weaver (2003), Factors contributing to diurnal temperature range
766 trends in twentieth and twenty-first century simulations of the CCCma coupled
767 model, *Climate Dyn.*, *20*, 435–445.

768 Venkatram, A., and R. Viskanta (1977), Radiative effects of elevated pollutant layers, *J.*
769 *Appl. Meteorol.*, *16*, 1256-1272, DOI: 10.1175/1520-
770 0450(1977)016<1256:REOEPL>2.0.CO;2.

771 Walko, R. L., L. E. Band, J. Baron, T. G. F. Kittel, R. Lammers, T. J. Lee, D. Ojima, R.
772 A. Pielke, C. Taylor, C. Tague, C. J. Treback, and P. L. Vidale (2000), Coupled
773 atmosphere-biophysics-hydrology models for environmental modeling, *J. Appl.*
774 *Meteorol.*, *39*, 931-944, DOI: 10.1175/1520-
775 0450(2000)039<0931:CABHMF>2.0.CO;2.

776 Walters, J. T., R. T. McNider, X. Shi, W. B. Norris, and J. R. Christy (2007), Positive
777 surface temperature feedback in the stable nocturnal boundary layer, *Geophys.*
778 *Res. Lett.*, *34*, L12709, doi:10.1029/2007GL029505.

779 Wang, J., and S. A. Christopher (2006), Mesoscale modeling of Central American smoke
780 transport to the United States: 2. Smoke radiative impact on regional surface
781 energy budget and boundary layer evolution, *J. Geophys. Res.*, *111*, D14S92,
782 doi:10.1029/2005JD006720.

783 Wang, J., S. A. Christopher, U. S. Nair, J. S. Reid, E. M. Prins, J. Szaykman, and J. L.
784 Hand (2006), Mesoscale modeling of Central American smoke transport to the

785 United States: 1. "Top-down" assessment of emission strength and diurnal
786 variation impacts, *J. Geophys. Res.*, *111*, D05S17, doi:10.1029/2005JD006416.

787 Welch, R., and W. Zdunkowski (1976), A radiation model of the polluted atmospheric
788 boundary layer, *J. Atmos. Sci.*, *33*, 2170-2184, DOI: 10.1175/1520-
789 0469(1976)033<2170:ARMOTP>2.0.CO;2.

790 Yu, H., S. C. Liu, and R. E. Dickinson (2002), Radiative effects of aerosols on the
791 evolution of the atmospheric boundary layer, *J. Geophys. Res.*, *107*(D12), 4142,
792 doi:10.1029/2001JD000754.

793 Zdunkowski, W. G., R. M. Welch, and J. Paegle (1976), One-dimensional numerical
794 simulation of the effects of air pollution on the planetary boundary layer, *J.*
795 *Atmos. Sci.*, *33*, 2399-2414, DOI: 10.1175/1520-0469(1976)033.

796 Zhou, L., R. E. Dickinson, Y. Tian, R. S. Vose, and Y. Dai (2007), Impact of vegetation
797 removal and soil aridation on diurnal temperature range in a semiarid region:
798 Application to the Sahel, *Proc. Natl. Acad. Sci.*, *104*, 17937-17942, doi:
799 10.1073/pnas.0700290104.

800 Zobler, L. (1999), Global Soil Types, 1-Degree Grid (Zobler). Data set. Available on-line
801 [<http://www.daac.ornl.gov>] from Oak Ridge National Laboratory Distributed
802 Active Archive Center, Oak Ridge, Tennessee, U.S.A.
803 doi:10.3334/ORNLDAAC/418.
804

Figure Legends

805

806 Figure 1. Comparison between observations (black line) and C1 simulation (red line) of:
807 a) downwelling shortwave; b) downwelling longwave; c) upwelling longwave; d)
808 sensible heat flux; e) latent heat flux; f) surface air temperature; and g) relative
809 humidity.

810 Figure 2. Comparison between C1 (red), D1 (green), U1 (blue), and X2 (black)
811 simulations. a) downwelling shortwave; b) downwelling longwave; c) surface air
812 temperature; and c) upwelling longwave.

813 Figure 3. Diurnal temperature range (open triangle), maximum (solid square) and
814 minimum (open circle) temperatures for the different experiments. The values are
815 valid for the time period including the first day and the second night.

816 Figure 4. Comparison between C1 (red) and U2 (blue) simulations for a) downwelling
817 longwave at the surface and b) surface air temperature.

818 Figure 5. Comparison between C1 (red) and U3 (blue) simulations for a) downwelling
819 longwave at the surface and b) surface air temperature.

820 Figure 6. Diurnal variation of aerosol extinction coefficient in the infrared (10.2-12.5
821 μm) in the U1 experiment at the first model level (solid line) and averaged for the
822 atmospheric column in the lowest 100 m.

823 Figure 7. Bifurcation diagrams with enhanced downward radiation from aerosols as the
824 bifurcation parameter (x axis) and boundary layer potential temperature as the
825 response variable (y axis) plotted along the x axis and the boundary layer
826 potential temperature. Line colors give roughness length: green – $z_0=0.1$ m, red –
827 $z_0 = 0.25$ m, pink - $z_0 = 0.5$ m, blue - $z_0 = 1.0$ m. (a) Bifurcation diagram for a

828 geostrophic wind speed of 3 m s^{-1} . (b) Bifurcation diagram for a geostrophic
829 wind speed of 7 m s^{-1} . (c) Bifurcation diagram for a geostrophic wind speed of 10
830 m s^{-1} .

831 Figure 8. Comparison between C2 (red) and U4 (blue) simulations for a) downwelling
832 longwave at the surface and b) surface air temperature.

833 Figure 9. Diurnal variation of: a) downwelling longwave radiation in U5 (black) and C3
834 (red) experiments; b) 2 m temperature, in U5 (black), C3 (red) and 3 hourly
835 observations (back dots); c) same as (a) except for U6 and C4 experiments and; d)
836 same as (b) except for U6 and C4 experiments.

837

838
839
840

TABLES

Aerosol Model	Composition			0.55 μm AOD (80% relative humidity)
	Component	Number Density (cm^{-3})	Mode radius (μm)	
Urban	Water Soluble	28,000	0.0212	0.643
	Insoluble	1.5	0.471	
	Soot	130,000	0.0118	
Urban [Panicker et al. 2008]	Water Soluble		0.0212	0.347
	Insoluble		0.471	
	Soot		0.0118	
Urban [Singh et al. 2005]	Soot	130,000	0.0118	0.863
	Water Soluble	10,000	0.0212	
	Mineral, Nucleation Mode	269.5	0.07	
	Mineral, Accumulation Mode	5.050	0.39	
	Mineral, Coarse Mode	3.850	1.90	
Desert	Water Soluble	0.018	0.0212	0.286
	Mineral, Nucleation mode	0.033	0.07	
	Mineral, Accumulation mode	0.747	0.39	
	Mineral, Coarse mode	0.202	1.90	

841
842
843
844
845
846
847
848
849
850
851
852
853
854
855

Table 1. Composition of aerosol models used in the study. Lognormal distribution is assumed for aerosol model components whose subcomponents are as follows: Water Soluble: Mixture of sulfates, nitrates and organics; Insoluble: Mixture of soil particles and organic material; Soot: Black carbon; Mineral: Mixture of quartz and clay [Hess et al., 1998].

856

Experiment Name	Description
C1	1D simulation initialized using CASES-99 radiosonde observation acquired at 0 UTC on 21 Oct 1999. Clear atmosphere and carbon dioxide concentration of 370 ppm (average value for 1999) are used.
U1	Same as C1 except for the assumption of urban aerosol loading.
U2	Same as U1 except for the assumption of zero nighttime AOD.
U3	Same as U1 except for the reduction of daytime AOD by a factor of 2.
X2	Same as C1 except for the assumption of doubling atmospheric CO ₂ concentration from present day values to 760 ppm.
D1	Same as C1 except for the assumption of desert dust aerosol loading.
C2	Same as C1 except for the assumption of constant soil saturation of 70%.
U4	Same as U1 except for the assumption of constant soil saturation of 70%.
U5	Urban land surface characteristics and aerosol optical characteristics deduced for Pune [<i>Panicker et al., 2008</i>]
C3	Same as U5 except for the assumption of an aerosol-free atmosphere.
U6	Urban land surface characteristics, aerosol optical characteristics deduced for New Delhi [<i>Singh et al., 2005</i>].
C4	Same as U6 except for the assumption of an aerosol-free atmosphere.

857

858

Table 2. Description of the numerical experiments utilized in this study.

859

860

861

862

863

864

865

866

Configuration	Experiments C1-C2, U1-U4, D1, X2	Experiments C3-C4, U5-U6
Vertical grid spacing at the surface	0.5 m	5 m
Grid stretch ratio	1.16	1.1
Maximum vertical grid spacing	500 m	500 m
Soil Levels (below ground)	0.05, 0.075, 0.15, 0.225, 0.375, 0.60, 0.90 m.	0.001, 0.05, 0.1, 0.2, 0.3, 0.5, 0.7 m
Soil Type	Clay Loam [<i>Chen et al., 2007</i>]	C3, U5: Sandy Soil C4, U6: Silt Loam [<i>Zobler, 1999</i>]
Land use	Short grass	Urban and built-up
Diffusion scheme [<i>Cotton et al., 2003</i>]	Vertical: Mellor-Yamada Horizontal: Modified Smagorinsky	Vertical: Mellor-Yamada Horizontal: Modified Smagorinsky
Initial atmospheric conditions	Radiosonde observations at 0 UTC (1800 LST)	Radiosnde observations at 1200 UTC (1730 LST)

867

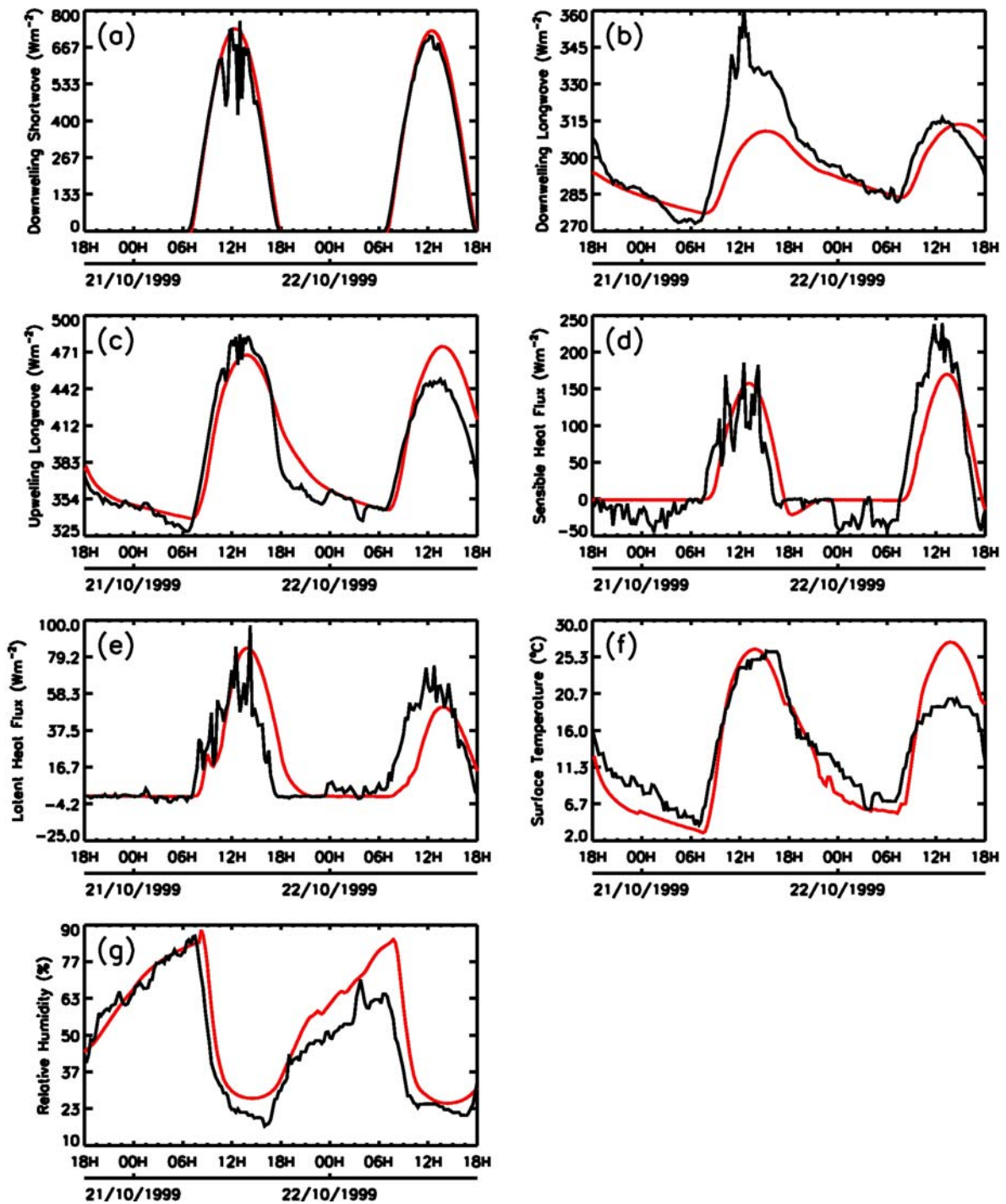
868

Table 3. Numerical model configuration used in the different experiments.

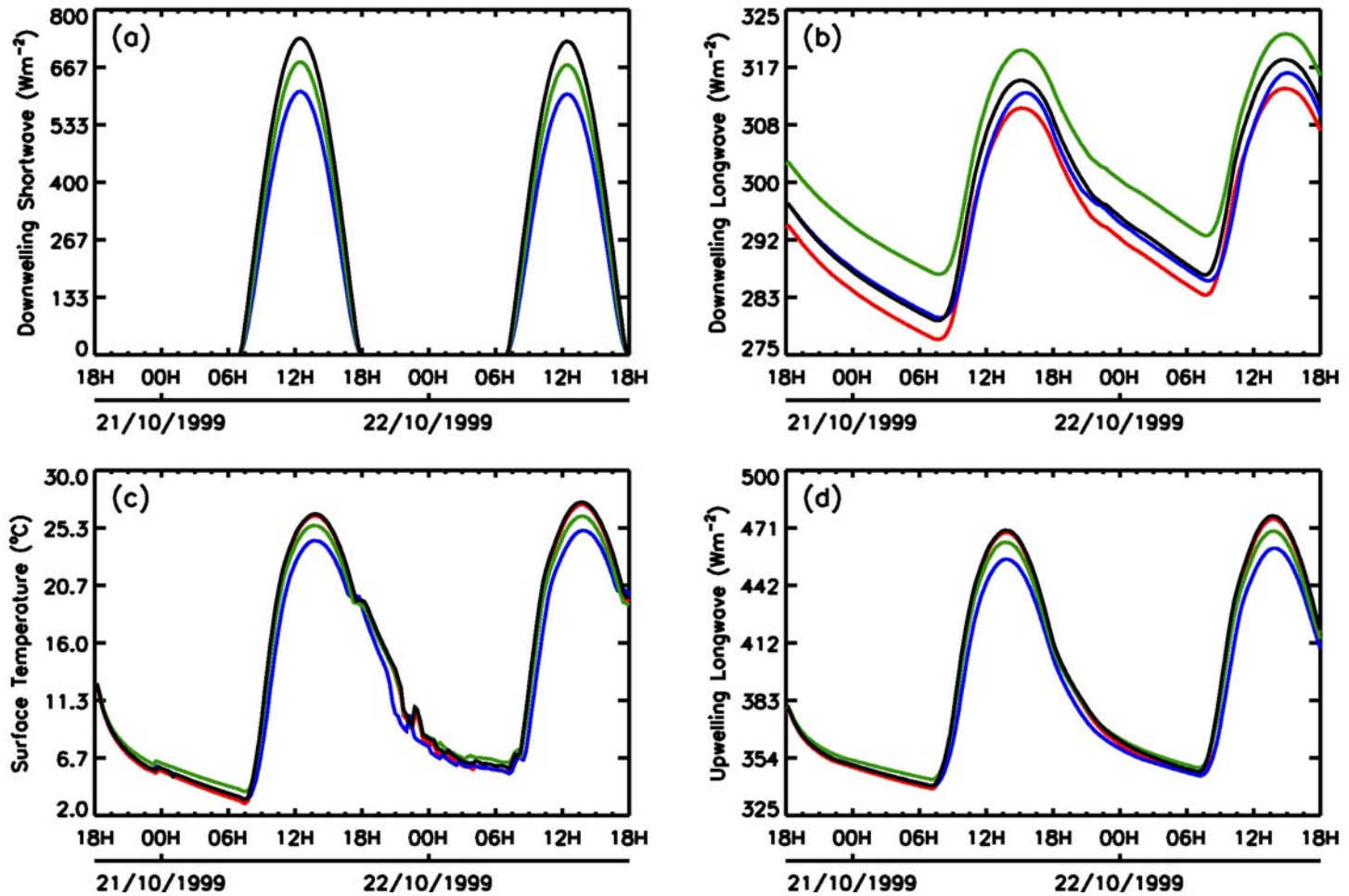
869

870

871

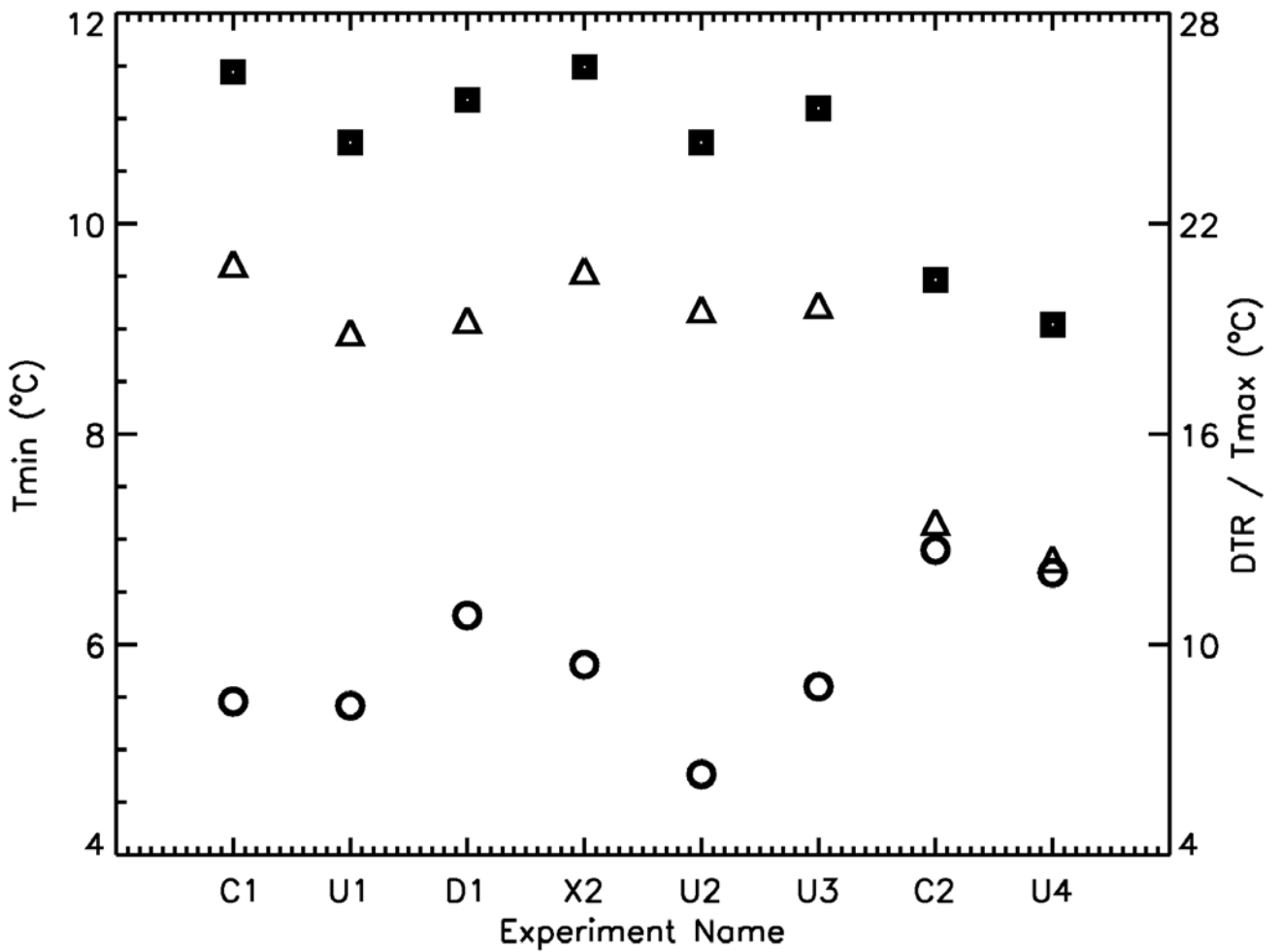


872
 873 Figure 1. Comparison between observations (black line) and C1 simulation (red line) of:
 874 a) downwelling shortwave; b) downwelling longwave; c) upwelling longwave; d)
 875 sensible heat flux; e) latent heat flux; f) surface air temperature; and g) relative
 876 humidity.



877
 878
 879
 880
 881
 882

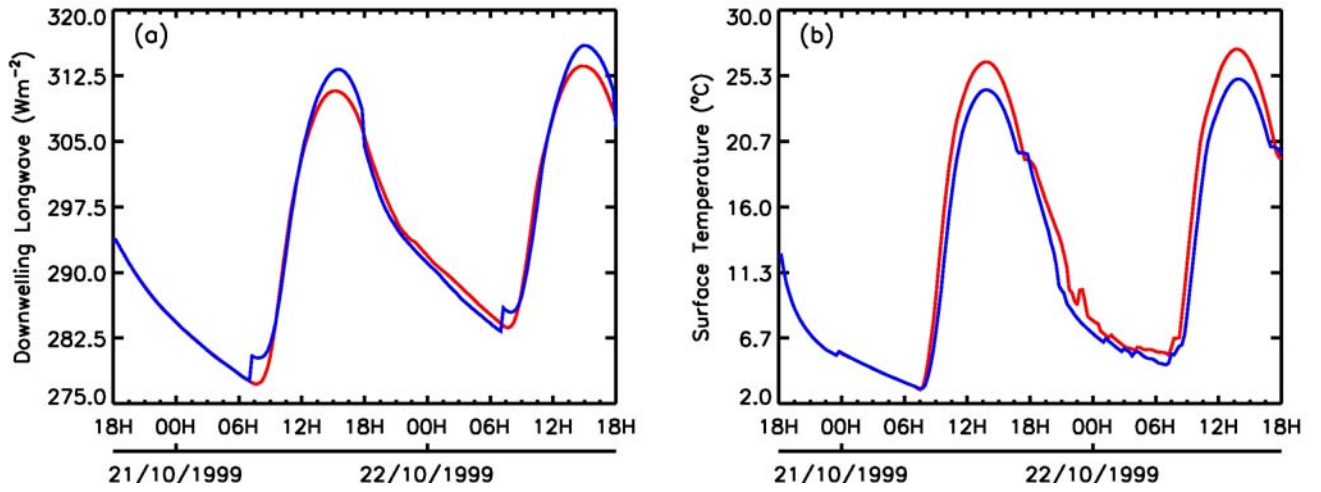
Figure 2. Comparison between C1 (red), D1 (green), U1 (blue), and X2 (black) simulations. a) downwelling shortwave; b) downwelling longwave; c) surface air temperature; and c) upwelling longwave. Note that in panel a, the differences between C1 and X2 are negligible and thus the curve for C1 (red) is hidden by the one for X2.



883
 884
 885
 886
 887
 888

Figure 3. Diurnal temperature range (open triangle), maximum (solid square), and minimum (open circle) temperatures for the different experiments. The values are valid for the time period including the first day and the second night.

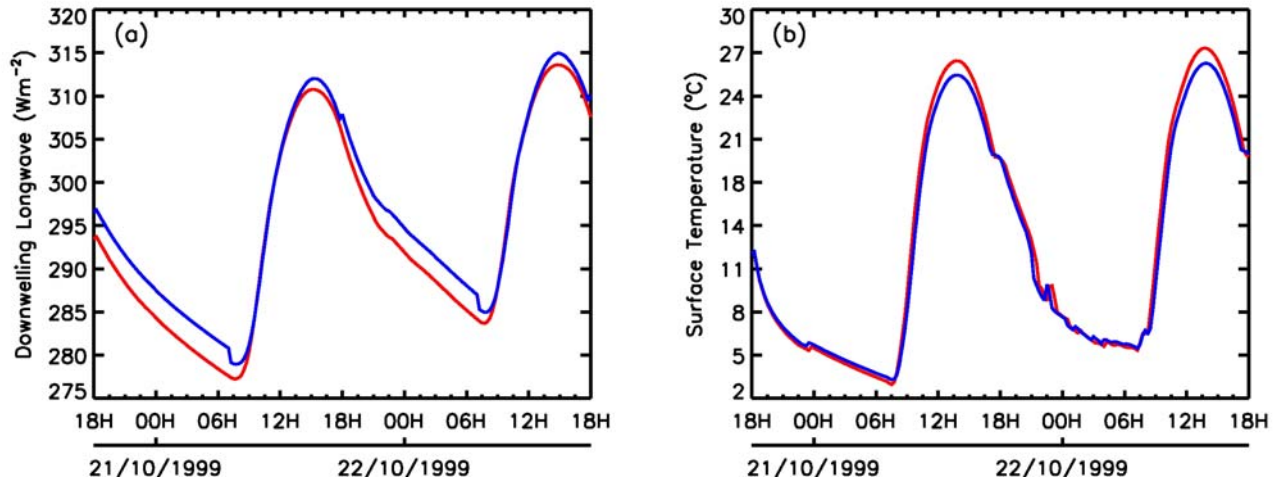
889
890
891
892
893
894
895



896
897
898
899
900
901
902
903
904
905
906
907
908
909
910
911
912
913
914
915
916
917
918

Figure 4. Comparison between C1 (red) and U2 (blue) simulations for a) downwelling longwave at the surface and b) surface air temperature.

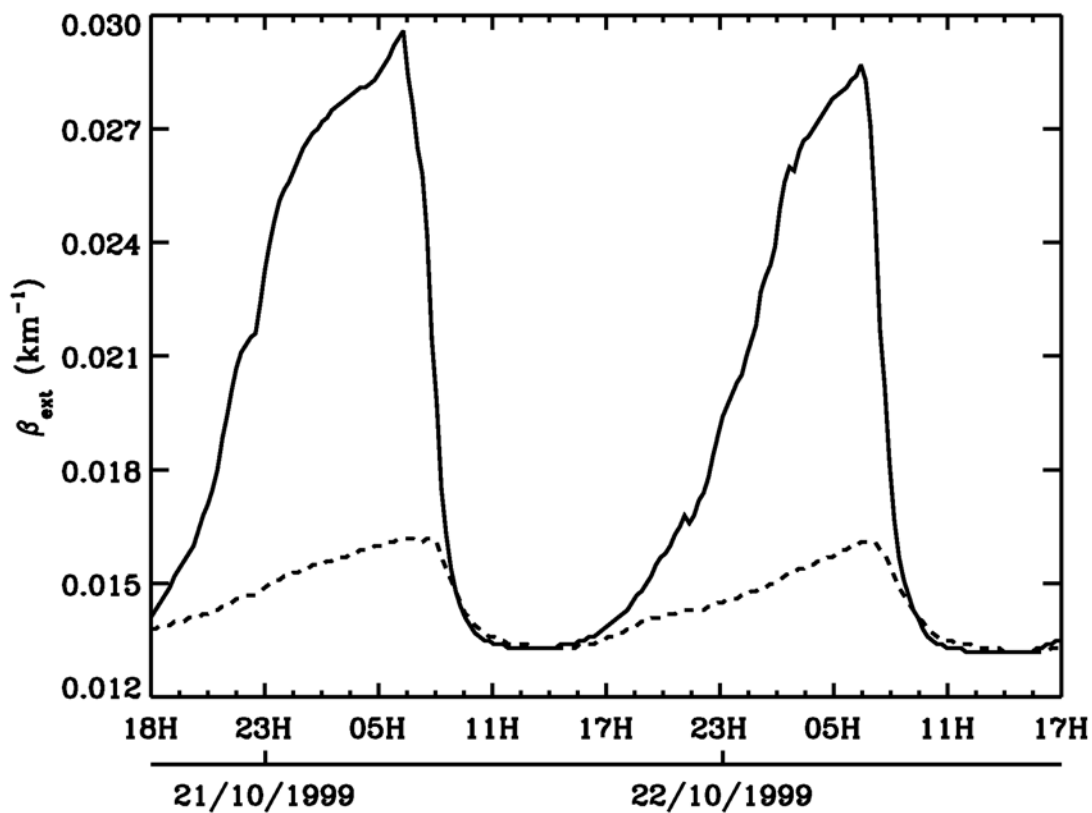
919
920
921
922
923
924



925
926
927
928
929
930
931
932
933
934
935
936
937
938

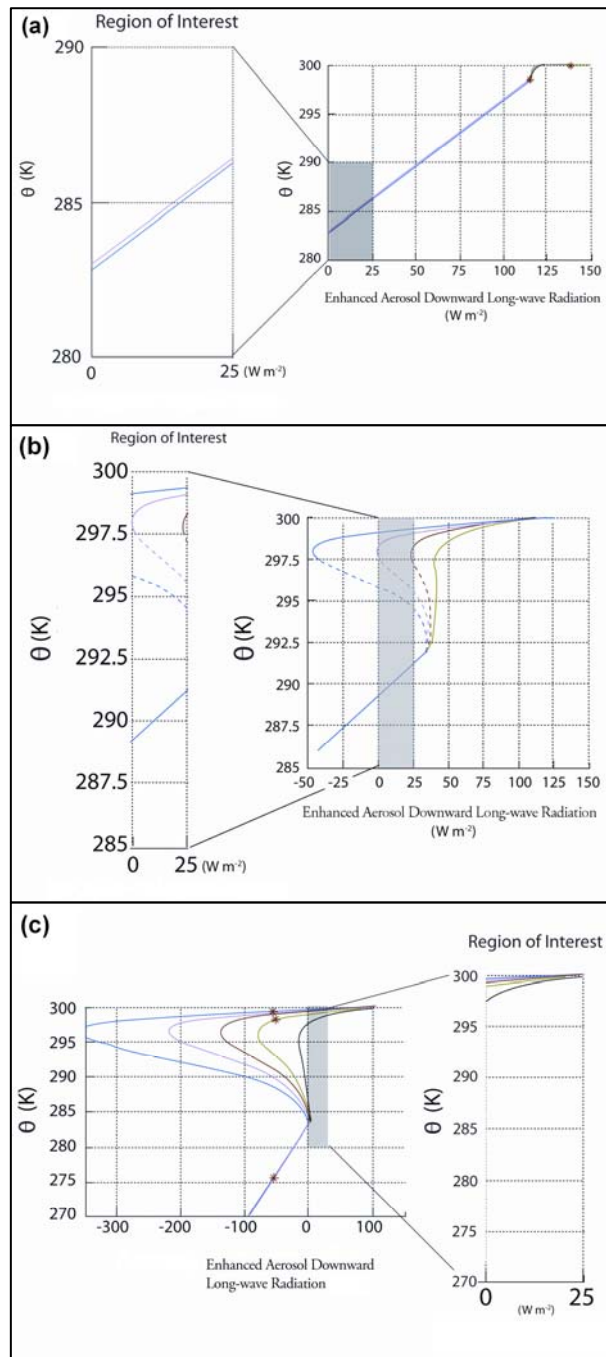
Figure 5. Comparison between C1 (red) and U3 (blue) simulations for a) downwelling longwave at the surface and b) surface air temperature.

939
940
941
942
943
944



945
946
947
948
949
950
951
952
953
954

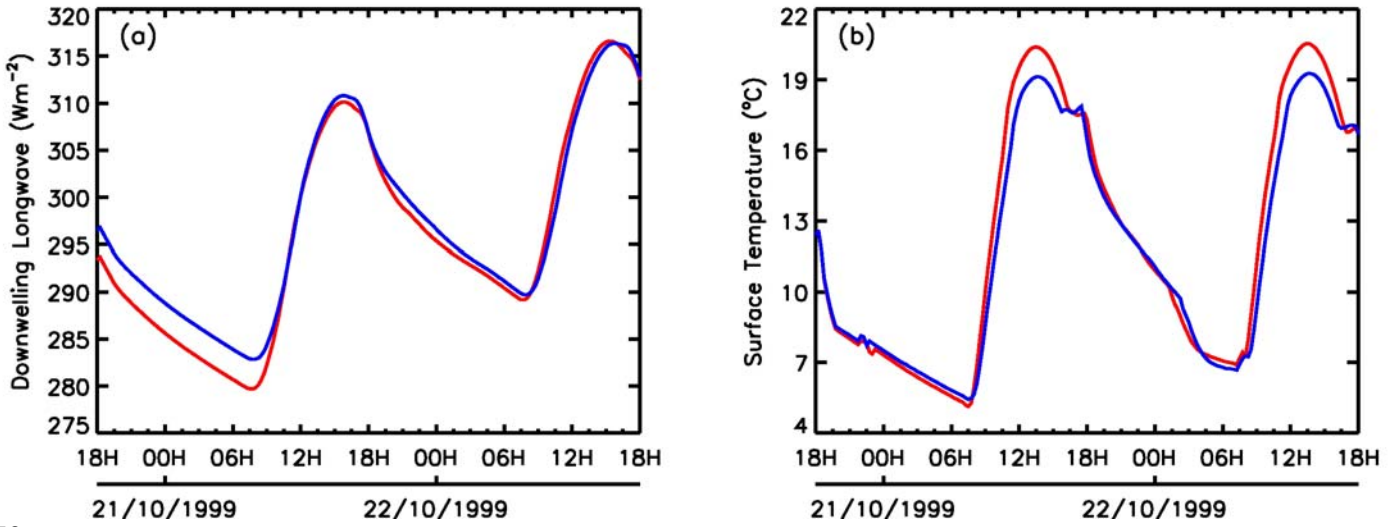
Figure 6. Diurnal variation of aerosol extinction coefficient in the infrared (10.2–12.5 μm) in the U1 experiment at the first model level (solid line) and averaged for the atmospheric column in the lowest 100 m.



956

957 Figure 7. Bifurcation diagrams with enhanced downward radiation from aerosols as the
 958 bifurcation parameter (x axis) and boundary layer potential temperature as the response
 959 variable (y axis) plotted along the x axis and the boundary layer potential temperature.
 960 Line colors give roughness length: green – $z_0=0.1 \text{ m}$, red – $z_0 = 0.25 \text{ m}$, pink - $z_0 = 0.5$
 961 m , blue - $z_0 = 1.0 \text{ m}$. (a) Bifurcation diagram for a geostrophic wind speed of 3 m s^{-1} . (b)
 962 Bifurcation diagram for a geostrophic wind speed of 7 m s^{-1} . (c) Bifurcation diagram for a
 963 geostrophic wind speed of 10 m s^{-1} .

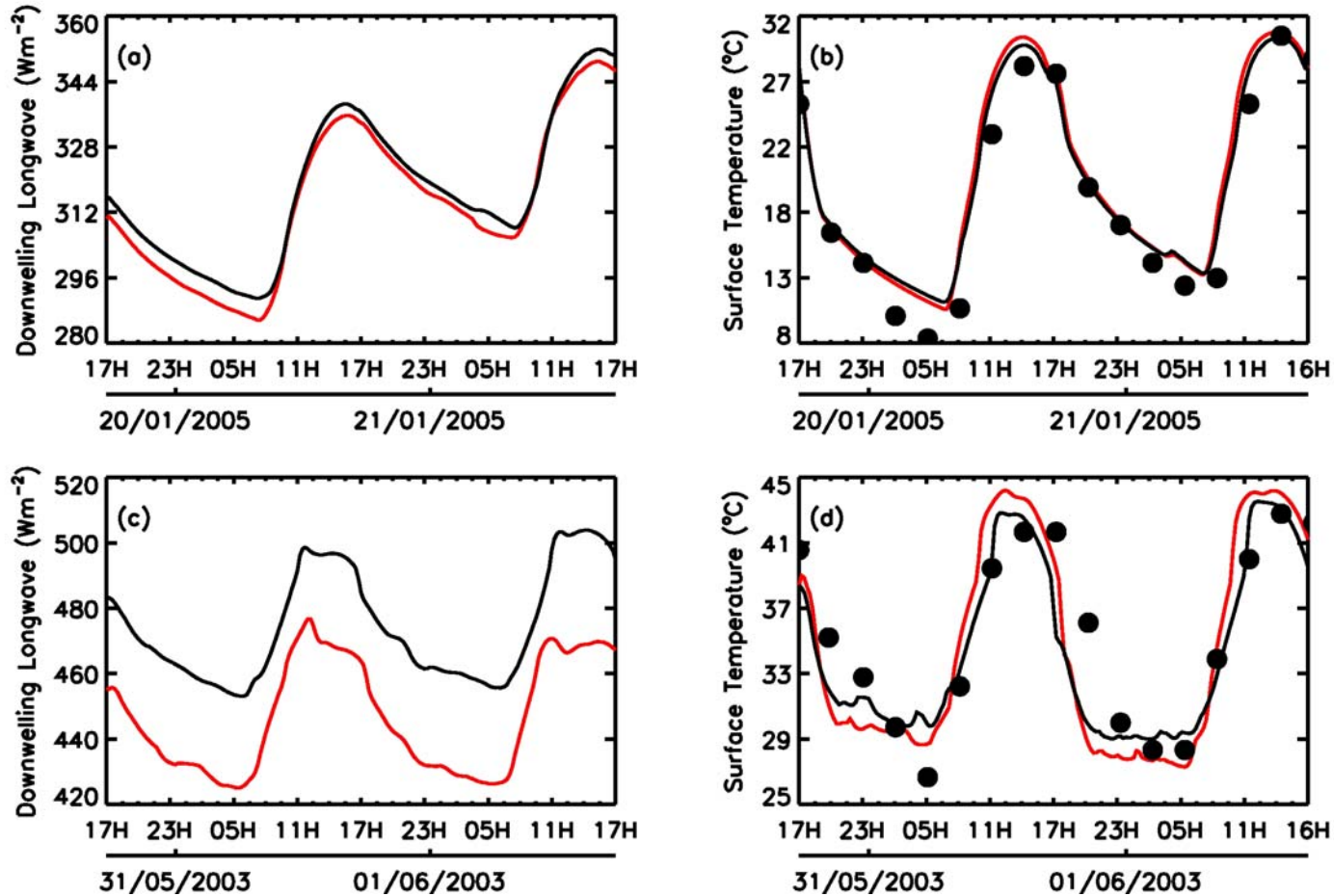
964
965
966
967
968
969



970
971
972
973
974

Figure 8. Comparison between C2 (red) and U4 (blue) simulations for a) downwelling longwave at the surface and b) surface air temperature.

975
976
977
978
979
980
981
982
983
984
985
986



988

989

990

991

Figure 9. Diurnal variation of: a) downwelling longwave radiation in U5 (black) and C3 (red) experiments; b) 2 m temperature, in U5 (black), C3 (red) and 3 hourly observations (back dots); c) same as (a) except for U6 and C4 experiments and; d) same as (b) except for U6 and C4 experiments.